STRUCTURAL BIOLOGY COMMUNICATIONS

ISSN 2053-230X

Structure of the AAVhu.37 capsid by cryoelectron microscopy

Jason T. Kaelber,[a]* Samantha A. Yost,[b] Keith A. Webber,[c] Emre Firlar,[a] Ye Liu,[b] Olivier Danos[b] and Andrew C. Mercer[b]*

[a]Institute of Quantitative Biomedicine and Rutgers New Jersey CryoEM/CryoET Core Facility, Rutgers, The State University of New Jersey, Piscataway, NJ 08854, USA, [b]Research and Early Development, REGENXBIO Inc., Rockville, MD 20850, USA, and [c]Technical Operations, REGENXBIO Inc., Rockville, MD 20850, USA. *Correspondence e-mail: jason.kaelber@rutgers.edu, amercer@regenxbio.com

Received 17 September 2019
Accepted 11 January 2020

Edited by A. K. Mitra, University of Auckland, New Zealand

Keywords: adeno-associated viruses; gene therapy; gene-delivery vectors; capsid; cryo-EM structure; AAVhu.37.

EMDB reference: AAVhu.37 capsid, EMD-20693

PDB reference: AAVhu.37 capsid, 6u95

Supporting information: this article has supporting information at journals.iucr.org/f

Adeno-associated viruses (AAVs) are used as *in vivo* gene-delivery vectors in gene-therapy products and have been heavily investigated for numerous indications. Over 100 naturally occurring AAV serotypes and variants have been isolated from primate samples. Many reports have described unique properties of these variants (for instance, differences in potency, target cell or evasion of the immune response), despite high amino-acid sequence conservation. AAVhu.37 is of interest for clinical applications owing to its proficient transduction of the liver and central nervous system. The sequence identity of the AAVhu.37 VP1 to the well characterized AAVrh.10 serotype, for which no structure is available, is greater than 98%. Here, the structure of the AAVhu.37 capsid at 2.56 Å resolution obtained via single-particle cryo-electron microscopy is presented.

1. Introduction

Adeno-associated viruses (AAVs), belonging to the *Dependoparvovirus* genus and the *Parvoviridae* family, are a group of small, non-enveloped, DNA viruses that are currently under intense study in the field of gene therapy (Mueller & Flotte, 2008; Daya & Berns, 2008). Their lack of pathogenicity and their ability to transduce both dividing and quiescent cells makes them promising candidates for the delivery of many clinically relevant cargoes; however, challenges remain regarding capsid engineering, including tissue-specific transduction, avoidance of the innate immune response and manufacturability (Mingozzi & High, 2011). The AAV capsid is composed of 60 subunits of viral protein assembled in a 25 nm icosahedral capsid that is capable of packaging a genome of approximately 4.7 kb (Berns & Parrish, 2015). Over 100 naturally occurring AAV serotypes and variants have been described and have been shown to have a variety of different properties (for example, packaging efficiency, biodistribution profile, stability *etc.*), which is largely attributed to the sequence diversity and conformational variability found in the variable-region (VR) loops located on the surface of the AAV capsid (Wu *et al.*, 2006). These AAV isolates have been organized into clades (A through F) according to their sequence similarity in the hope of identifying important sequences contributing to the similar functional characteristics of a group (Gao *et al.*, 2004).

The clade E serotype AAVhu.37 efficiently transduces the liver in mouse models and nonhuman primates (NHP) after intravenous injection (Wang, Wang *et al.*, 2010; Greig *et al.*, 2018). When injected directly into mouse brain, AAVhu.37

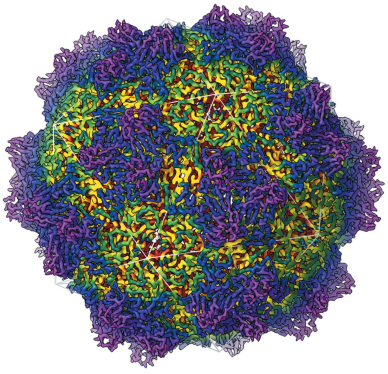

also transduces the central nervous system (CNS; Cearley *et al.*, 2008). AAVhu.37 is 98.5% identical to AAVrh.10 and differs by only one amino acid (VP1 residue 24) from AAVrh.39. AAVrh.10 (Zhang *et al.*, 2011; Yang *et al.*, 2014) and AAVrh.39 (Lawlor *et al.*, 2009) cross the blood–brain barrier (BBB) and efficiently transduce NHP CNS tissues (Rosenberg *et al.*, 2014). Although the BBB-penetrating capacity of AAVhu.37 has not been assayed in published work, it is likely that the structural motifs in AAVhu.37 that are responsible for BBB penetration would be identical to those in AAVrh.39 and AAVrh.10. In a preclinical study for the treatment of hemophilia A, macaques administered with AAVhu.37 carrying a functional human blood coagulation factor VIII (hFVIII) gene linked to E03.TTR (liver-specific) promoter exhibited high levels of hFVIII circulating in the blood (Greig *et al.*, 2018). While hepatic gene transfer can induce immunity to the transferred gene (Dobrzynski *et al.*, 2006), hepatic gene transfer with AAV can induce immune tolerance (Mount *et al.*, 2002; Mingozzi *et al.*, 2003; Breous *et al.*, 2009, 2011), even when the gene transfer is not systemic (Martino *et al.*, 2009). There is an effect of the serotype on the immune tolerance level (Greig *et al.*, 2017), and AAVhu.37 has favorable tolerance and expression effects (Greig *et al.*, 2018). This study has been further extended into an ongoing clinical trial (ClinicalTrials.gov NCT03588299; https://clinicaltrials.gov/). Furthermore, AAVhu.37 has been reported to be favorable for high-yield, scalable manufacturing, and it binds AVB resin, providing a simple purification strategy (Wang *et al.*, 2015; Greig *et al.*, 2018).

In order to further understand the structure–function relationship of AAV capsid variants across serotypes, we sought to describe the structure of the clinically relevant capsid AAVhu.37.

2. Materials and methods

2.1. Vector production

AAVhu.37 (GenBank AAS99285.1) particles containing ssDNA with a CAG promoter and encoding green fluorescent protein (GFP) were produced by triple transfection of adherent HEK293T cells. Vector particles were harvested via freeze–thawing and purified via an iodixanol gradient (Zolotukhin *et al.*, 1999). The final product was resuspended in phosphate-buffered saline (PBS) and 0.001% Pluronic F-68. The genome titer was determined via Droplet Digital PCR (ddPCR) using primers against the rabbit β-globin polyadenylation signal of the transgene sequence as described previously (Lock *et al.*, 2014).

2.2. Composition and purity analysis

The capsid-protein purity and the ratio of relative mass of the capsid proteins were determined by capillary gel electrophoresis. The AAV sample was denatured and reduced by heating in a solution containing sodium dodecyl sulfate and dithiothreitol. The sample was diafiltered to remove excess salt and was then electrokinetically injected into a gel-filled capillary using a PA800 Plus (SCIEX) instrument. The capsid proteins were separated based on size by applying a voltage to the capillary. Detection and quantitation of the capsid proteins were performed using detection at 214 nm.

For intact LC-MS determination, the sample was injected into a Vanquish UHPLC coupled to a Q Exactive HF-X Hybrid Quadrupole-Orbitrap mass spectrometer (Thermo Fisher Scientific). The separation was performed on a UPLC BEH C4 column using reversed-phase chromatography. Proteins were deconvolved with *Intact Mass* v.3.6 from Protein Metrics. LC-MS/MS of digested peptides was performed as described previously (Cai *et al.*, 2017). Peptides were searched against a database containing human UniProt sequences, common contaminants such as porcine trypsin and AAVhu.37.

Table 1
Cryo-electron microscopy.

Defocus range (90%) (nm)	350–1720
Pixel size at specimen (Å)	1.038
Super-resolution pixel size at the specimen (Å)	0.519
Total dose (e Å^{-2})	∼32.8
Frame rate (frames per second)	5
Micrographs collected	736
Particles extracted	52235
Particles in final reconstruction	41849
Guinier plot *B* factor (Å^2)	113
Resolution at FSC = 0.143	
Unmasked	2.80
Masked	2.53
Noise-corrected ('true FSC')	2.56

Table 2
Model refinement.

No. of non-H protein atoms	4125
No. of ligand atoms	0
Average *B* factor (Å^2)	34
R.m.s. deviations	
Bonds (A°)	0.0078
Angles (°)	1.07
Validation	
MolProbity score	1.42
Clashscore	7.11
Rotamer outliers	1 (0.2%)
Ramachandran plot	
Favored regions	506 (98%)
Additionally allowed	10 (2%)
Outliers	1 (0.2%)

2.3. CryoEM sample preparation and data collection

Pluronic F-68 was removed before vitrification by diafiltration with seven washes with PBS using an Amicon Ultra-0.5 100 kDa molecular-weight cutoff regenerated cellulose spin column (Sigma–Aldrich). Amorphous carbon film was deposited on cleaved V1 mica (Ted Pella, Redding, California, USA) by E-beam deposition using an ACE600 (Leica Microsystems GmbH) and the carbon thickness as measured by the quartz-crystal oscillation method was 2.86 nm. Carbon was floated on glow-discharged Quantifoil R2/1 grids (Quantifoil Micro Tools GmbH) within an hour of vitrification. 3.5 µl of particles diluted in PBS was applied to the grid and plunge-frozen using an EM-GP (Leica Microsystems GmbH) with

Whatman No. 1 blotting paper (Sigma–Aldrich). The grid used for the final data set was blotted for 4.5 s.

Grids were imaged (Table 1) on a Talos Arctica cryo-electron microscope aligned as described previously (Herzik *et al.*, 2017), except that *AutoCTF* and *EPU* (Thermo Fisher Scientific) were employed instead of *Leginon*. Images were recorded with a K2 Summit detector (Gatan) in super-resolution mode. To evaluate the presence of the genome, 15 micrographs from throughout the final data set were high-pass (1000 Å) and low-pass (28.5 Å) filtered and 1074 particles were manually scored. The mean of means for the 15 fields of view differed from the overall mean by less than 0.1%.

2.4. Map reconstruction

Movies were processed with dose-weighting and rebinned to 1.038 Å per pixel using *MotionCor*2 (Zheng *et al.*, 2017). Particles were boxed with *EMAN*2 (Tang *et al.*, 2007). Extracted particles were imported into *cryoSPARC*2 and icosahedral *ab initio* refinement generated a data-derived

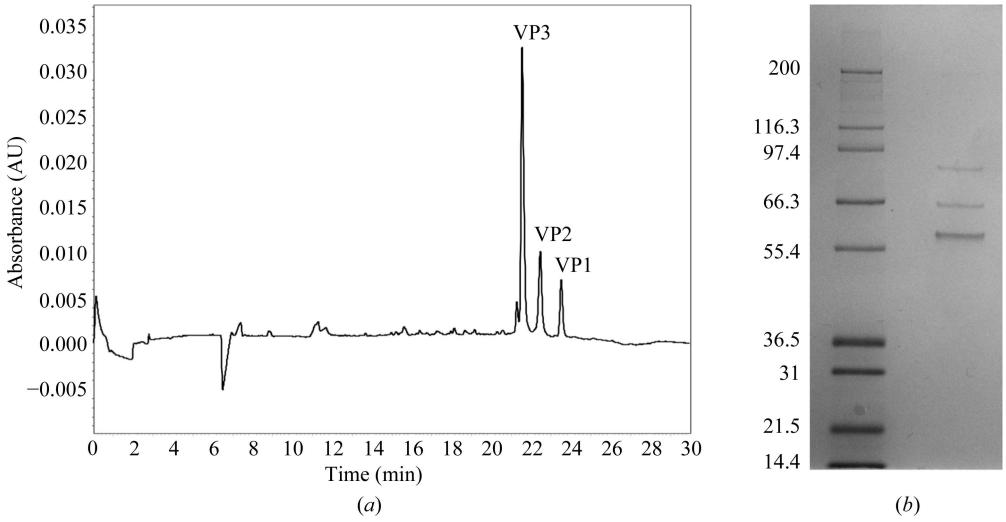

Figure 1
(*a*) Capillary gel electrophoretic separation of an AAVhu.37 sample illustrating the presence of VP1, VP2 and VP3 proteins in the sample. (*b*) SDS–PAGE gel of AAVhu.37 from which three bands were cut for LC-MS/MS of the digested peptides.

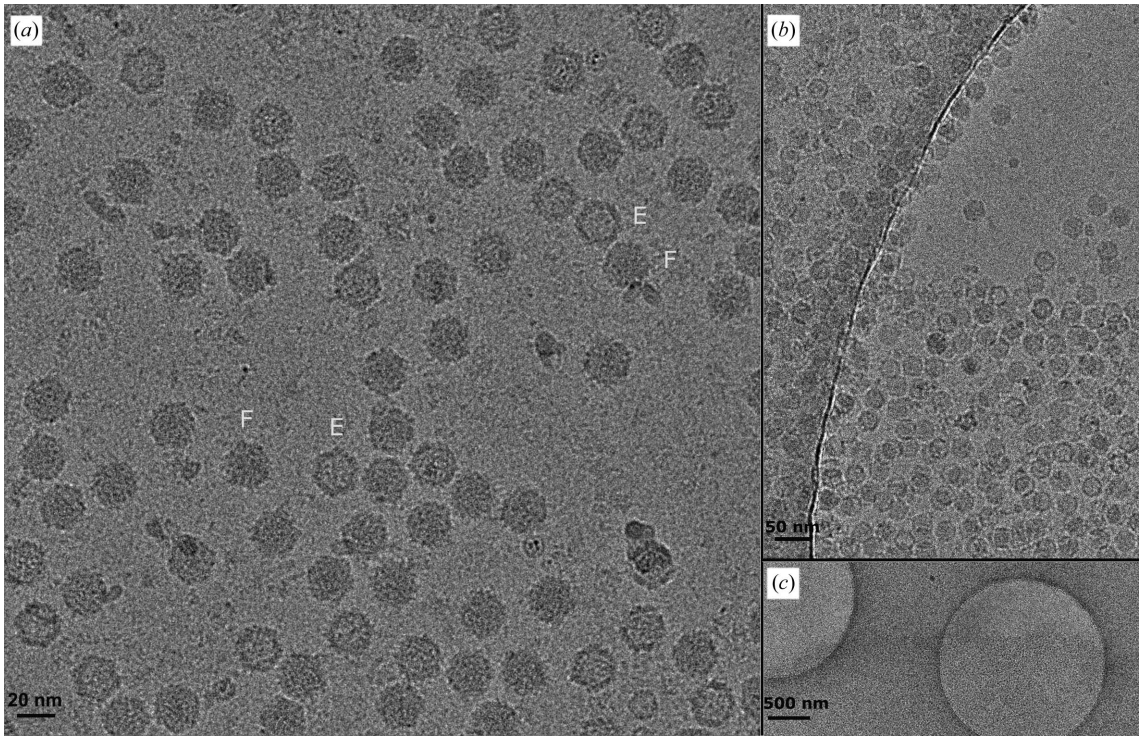

Figure 2
(*a*) One randomly selected micrograph from the final data set, low-pass filtered to 8 Å resolution for display. Exemplars are labeled in cyan to represent full capsids (F) and empty capsids (E). (*b*) A screening micrograph in which the edge of the thin amorphous film is suspended over a hole in the carbon foil illustrates the concentrating effect of the film on the particle count. (*c*) The same field of view at lower magnification.

initial model (Punjani *et al.*, 2017). The structure was refined to 2.8 Å resolution with icosahedral symmetry, the handedness was flipped with reference to known parvoviral structures and a mask was generated from the structure using *EMAN*2. The movies were corrected again, rebinned to 0.83 Å per pixel in *RELION* and further refinement was pursued in both *RELION* and *cryoSPARC*: both methods produced maps that were identical by eye. The deposited map was generated by performing particle polishing in *RELION* (Zivanov *et al.*, 2019) and homogeneous refinement in *cryoSPARC*. This map has a Fourier shell correlation (FSC) of 0.143 at 2.56 Å resolution. Representative density for residues 622–635 is shown in Fig. 3(*c*). We note that the resolution at FSC = 0.143 for the latter map reconstruction is greater than three times the voxel length, so it satisfies the '2/3 Nyquist criterion' of van Heel (Orlova *et al.*, 1997). In no step of map generation was a model used from any other data set.

2.5. Model refinement

AAV8 (PDB entry 2qa0; Nam *et al.*, 2007) was used as an initial template for modeling and had a high fit to density even before refinement. Rounds of automatic refinement in *Phenix* and manual refinement in *Coot* (Liebschner *et al.*, 2019; Emsley *et al.*, 2010) were conducted and the final coordinates (Table 2) were evaluated by eye and using *MolProbity* (Chen *et al.*, 2010). Structural figures were generated using *PyMOL* (v.2.1.0; Schrödinger) or *UCSF Chimera* (Pettersen *et al.*, 2004).

3. Results and discussion

3.1. AAVhu.37-GFP particles

Purified AAVhu.37-GFP was titered via ddPCR against the transgene to a concentration of 7.5×10^{12} genome copies per millilitre. Capillary gel electrophoresis yielded three major peaks (Fig. 1). This reflects the generally known capsid composition of AAVs, where the capsids comprise a mixture of VP1, VP2 and VP3, with VP3 predominating (Rose *et al.*, 1971). VP2 and VP3 are N-terminal truncations of VP1; the VP3 region is common to all three forms. The absence of other significant peaks indicates a high purity.

We confirmed that VP1, VP2 and VP3 are the significant components of this preparation by mass spectrometry.

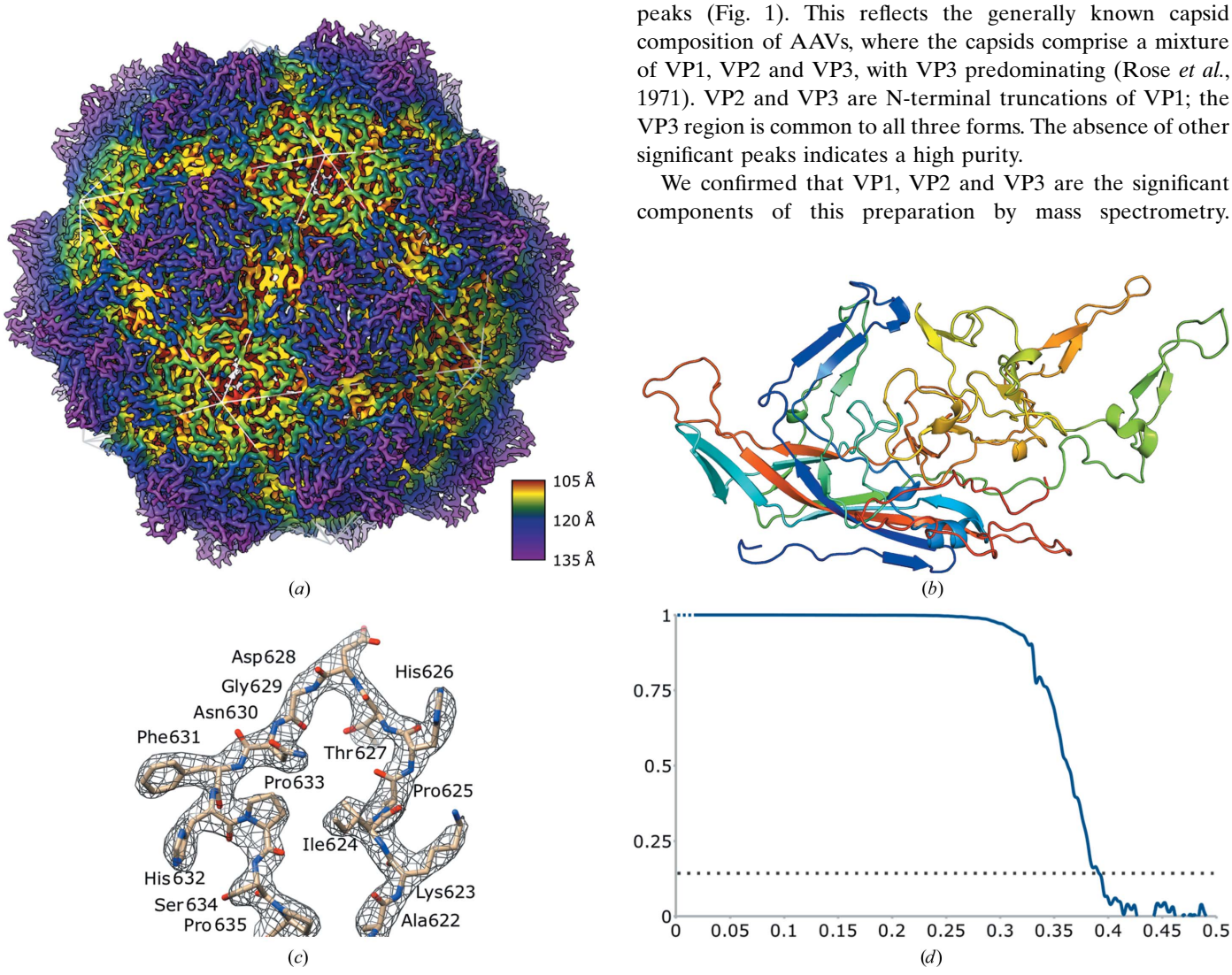

Figure 3
(*a*) Overall capsid-surface model colored radially, with the icosahedral geometry indicated by a white-lined overlay. (*b*) Model of a single VP3 monomer colored from the N-terminus (blue) to the C-terminus (red). (*c*) Representative map section allowing unambiguous tracing of the AAVhu.37 backbone. (*d*) Noise-corrected Fourier shell correlation plotted against spatial frequency ($Å^{-1}$) between the two half-maps of the final refinement iteration, with FSC = 0.143 indicated by a dotted line. Note that the low-resolution terms are not independent.

Reversed-phase chromatography of intact capsids detected unfragmented masses matching the predicted masses of VP3 (measured 59 666.4 Da, predicted 59 667.6 Da), VP2 (measured 66 284.9 Da, predicted 66 286.0 Da) and VP1 (measured 81 491.8 Da, predicted 81 492.6 Da). SDS–PAGE analysis of the sample revealed exactly three bands (Fig. 1*b*). An in-gel digest of these bands (Fig. 1*b*) followed by LC-MS/MS identified all three bands as AAV capsid protein based on the presence of peptides from the shared (VP3) region. Additionally, VP1-unique peptides were detected from the highest molecular-weight band. In each of the three bands, AAV capsid protein predominated. The low-abundance contaminants mainly consisted of porcine trypsin, human heat-shock proteins and keratin.

On vitrified EM grids, particles preferentially partitioned to carbon surfaces even when the solvent layer in bare holes was thick. A thin, amorphous carbon film increased the effective particle concentration (Fig. 2). 82.0% of the particles contained DNA (full or partially full), 16.3% were empty and 1.7% of the particles were insufficiently resolved to unambiguously determine the presence of the genome.

3.2. Overall AAVhu.37 structure

The AAVhu.37 map had an overall resolution of 2.56 Å, allowing the modeling of residues 220–738 (VP1 numbering) of the full-length capsid protein, as is typical of previously described AAV capsid structures (Fig. 3). The inability to resolve the complete N-terminus using current structure-determination methods is thought to be owing to particle-to-particle variability of the VP1 and VP2 copy number, non-uniform N-terminal orientation within the AAV capsids and areas of potential structural flexibility. A plug of density not accounted for by the model was observed in the fivefold pore beginning at a radius of 9.0 nm and terminating at a radius of 10.0 nm from the capsid center. The residues surrounding this plug were well ordered. This phenomenon is not uncommon in icosahedral maps of *Parvoviridae* (Subramanian *et al.*, 2017) and may correspond to the presence of the VP1 N-terminus in an asymmetric configuration and/or ordered ions or solvent. The overall fold of the AAVhu.37 capsid is consistent with other AAV serotypes as well as with more distantly related parvovirus groups (Fig. 3*b*; Mietzsch *et al.*, 2019).

Intermediate-voltage microscopes are increasingly being utilized for high-resolution work. The structure described here is of higher resolution than any other peer-reviewed single-particle cryoEM structure from a 200 kV electron microscope to date, albeit by 0.03 Å (Herzik *et al.*, 2017). Preprinted work

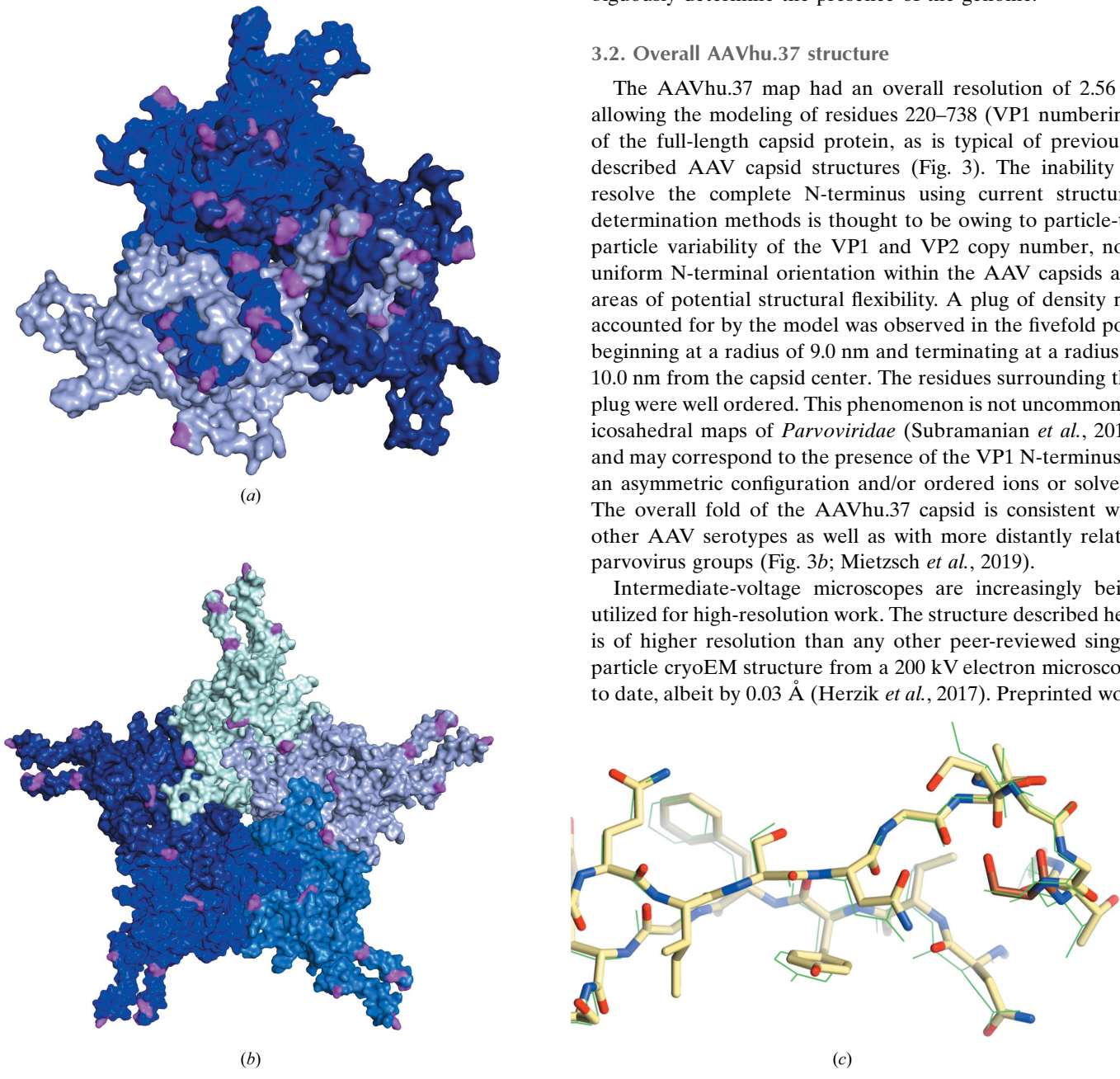

(*a*) (*b*) (*c*)

Figure 4
AAVhu.37 VP3 monomers shown in shades of blue, highlighting amino-acid differences (pink) between AAVhu.37 and AAVrh.10 relative to the (*a*) threefold and (*b*) fivefold axes of symmetry. (*c*) Comparison of the VR-I loop of AAV8 (shown in green as lines) and AAVhu.37 (shown as sticks with C atoms colored yellow; amino acids 262–275). Residue 269, the single amino-acid difference in VR-I between the two serotypes, is indicated by darker coloring (orange C atoms).

indicates that resolutions of beyond 2 Å are attainable using commercially available 200 kV microscopes (Wu *et al.*, 2019).

3.3. Comparison to known serotypes

Of the released structures within the Protein Data Bank (PDB), AAV8 is the most closely related capsid to AAVhu.37, with 93.5% amino-acid identity for full-length VP1. Although several AAV8 capsid structures exist in the literature, the most directly comparable entry, PDB entry 3ra4 (Nam *et al.*, 2011), is an AAV8 capsid containing a GFP-encoding genome determined at pH 7.5 via X-ray crystallography to 2.7 Å resolution. The overall calculated r.m.s.d. of the two structures is 0.564 Å. Of the 39 amino-acid differences in VP3 between these two serotypes, 18 (46%) are in the variable-region (VR) loops that form the spikes surrounding the threefold axis of symmetry (Mietzsch *et al.*, 2019): nine in VR-IV, four in VR-V and five in VR-VIII. The r.m.s.d.s for VR-IV (amino acids 449–477), VR-V (amino acids 493–512) and VR-VIII (amino acids 578–600) are 0.422, 0.326 and 0.302 Å, respectively. In other serotypes, these areas are known to be hotspots for binding cellular protein receptors and glycan receptors, as well as neutralizing antibodies (Zhang *et al.*, 2019; Meyer *et al.*, 2019; Bell *et al.*, 2012; O'Donnell *et al.*, 2009; Giles *et al.*, 2018; Huang *et al.*, 2016; Tseng & Agbandje-McKenna, 2014). Although VR-VIII has the lowest amino-acid identity of any region between AAVhu.37 and AAV8 (70%), the main chain is scarcely perturbed.

The AAVrh.10 capsid, the structure of which has not been solved, and AAVhu.37 share 98.5% amino-acid identity. Mapping AAVrh.10 residues onto the AAVhu.37 structure reveals a clustering of differential amino acids at the spikes surrounding the threefold axis of symmetry, which may be responsible for its decreased immunogenicity (Greig *et al.*, 2018; Wang, Calcedo *et al.*, 2010; Figs. 4*a* and 4*b*). Determinants of BBB penetration have been mapped to VR-I by making chimeric capsids between the BBB-penetrating AAVrh.10 and the nonpenetrating AAV1 (Albright *et al.*, 2018). The AAVrh.10 VR-I residues that were identified as sufficient to confer BBB penetration on AAV1 are absolutely conserved in AAVhu.37. The VR-I of the nonpenetrating AAV8 differs at only one site: AAVhu.37 and AAVrh.10 contain a serine at position 269, while AAV8 contains an alanine. Superimposition of AAVhu.37 with previously published structures of AAV8 (Nam *et al.*, 2007, 2011) reveals no evidence of differences in the VR-I loop conformation (Fig. 4*c*). An important caveat is that VR-I of AAV2 rearranges during AAV receptor (AAVR) engagement (Meyer *et al.*, 2019). Bound AAVR would sterically clash with VR-I of AAVhu.37 unless it was pushed aside during binding. Hence, we cannot exclude the possibility that the serine/alanine polymorphism could lead to a biologically relevant difference in loop flexibility or in a cofactor-engaged structure. On balance, we hypothesize that while splicing an AAVrh.10 VR-I epitope into AAV1 may be sufficient to confer BBB penetration to AAV1, one or more additional AAV8-specific factors are likely to block BBB penetration. This finding encourages further inspection of capsid elements which may confer or inhibit the ability to cross the BBB and promotes the rational design of novel capsids for more efficient BBB penetration.

Acknowledgements

We thank Haiyan Zheng and Amenah Soherwardy at the Rutgers Biological Mass Spectrometry Facility for digested LC-MS/MS. We thank the REGENXBIO analytical development department for their support on this project: Vurghun Ahmadov for capillary gel electrophoresis, Shugui Chen for undigested LC-MS, Tomoko Maekawa for ddPCR, and Zhuchun Wu and Zhenhong Li for technology development and oversight. We would also like to thank April Giles for bioinformatic analysis of the capsid sequence.

Funding information

This work was funded by REGENXBIO (grant to Jason T. Kaelber).

References

Albright, B. H., Storey, C. M., Murlidharan, G., Castellanos Rivera, R. M., Berry, G. E., Madigan, V. J. & Asokan, A. (2018). *Mol. Ther.* **26**, 510–523.
Bell, C. L., Gurda, B. L., Van Vliet, K., Agbandje-McKenna, M. & Wilson, J. M. (2012). *J. Virol.* **86**, 7326–7333.
Berns, K. I. & Parrish, C. R. (2015). *Fields Virology*, 6th ed., edited by D. M. Knipe & P. M. Howley, pp. 1768–1791. Philadelphia: Lippincott Williams & Wilkins.
Breous, E., Somanathan, S., Bell, P. & Wilson, J. M. (2011). *Gastroenterology*, **141**, 348–357.
Breous, E., Somanathan, S., Vandenberghe, L. H. & Wilson, J. M. (2009). *Hepatology*, **50**, 612–621.
Cai, N., Bai, Z., Nanda, V. & Runnels, L. W. (2017). *Sci. Rep.* **7**, 42739.
Cearley, C. N., Vandenberghe, L. H., Parente, M. K., Carnish, E. R., Wilson, J. M. & Wolfe, J. H. (2008). *Mol. Ther.* **16**, 1710–1718.
Chen, V. B., Arendall, W. B., Headd, J. J., Keedy, D. A., Immormino, R. M., Kapral, G. J., Murray, L. W., Richardson, J. S. & Richardson, D. C. (2010). *Acta Cryst.* D**66**, 12–21.
Daya, S. & Berns, K. I. (2008). *Clin. Microbiol. Rev.* **21**, 583–593.
Dobrzynski, E., Fitzgerald, J. C., Cao, O., Mingozzi, F., Wang, L. & Herzog, R. W. (2006). *Proc. Natl Acad. Sci. USA*, **103**, 4592–4597.
Emsley, P., Lohkamp, B., Scott, W. G. & Cowtan, K. (2010). *Acta Cryst.* D**66**, 486–501.
Gao, G., Vandenberghe, L. H., Alvira, M. R., Lu, Y., Calcedo, R., Zhou, X. & Wilson, J. M. (2004). *J. Virol.* **78**, 6381–6388.
Giles, A. R., Govindasamy, L., Somanathan, S. & Wilson, J. M. (2018). *J. Virol.* **92**, e01011-18.
Greig, J. A., Nordin, J. M. L., White, J. W., Wang, Q., Bote, E., Goode, T., Calcedo, R., Wadsworth, S., Wang, L. & Wilson, J. M. (2018). *Hum Gene Ther.* **29**, 763–770.
Greig, J. A., Wang, Q., Reicherter, A. L., Chen, S.-J., Hanlon, A. L., Tipper, C. H., Clark, K. R., Wadsworth, S., Wang, L. & Wilson, J. M. (2017). *Hum. Gene Ther.* **28**, 392–402.
Herzik, M. A. Jr, Wu, M. & Lander, G. C. (2017). *Nat. Methods*, **14**, 1075–1078.
Huang, L. Y., Patel, A., Ng, R., Miller, E. B., Halder, S., McKenna, R., Asokan, A. & Agbandje-McKenna, M. (2016). *J. Virol.* **90**, 5219–5230.
Lawlor, P. A., Bland, R. J., Mouravlev, A., Young, D. & During, M. J. (2009). *Mol. Ther.* **17**, 1692–1702.

Liebschner, D., Afonine, P. V., Baker, M. L., Bunkóczi, G., Chen, V. B., Croll, T. I., Hintze, B., Hung, L.-W., Jain, S., McCoy, A. J., Moriarty, N. W., Oeffner, R. D., Poon, B. K., Prisant, M. G., Read, R. J., Richardson, J. S., Richardson, D. C., Sammito, M. D., Sobolev, O. V., Stockwell, D. H., Terwilliger, T. C., Urzhumtsev, A. G., Videau, L. L., Williams, C. J. & Adams, P. D. (2019). *Acta Cryst.* D**75**, 861–877.
Lock, M., Alvira, M. R., Chen, S.-J. & Wilson, J. M. (2014). *Human Gene Therapy Methods*, **25**, 115–125.
Martino, A. T., Nayak, S., Hoffman, B. E., Cooper, M., Liao, G., Markusic, D. M., Byrne, B. J., Terhorst, C. & Herzog, R. W. (2009). *PLoS One*, **4**, e6376.
Meyer, N. L., Hu, G., Davulcu, O., Xie, Q., Noble, A. J., Yoshioka, C., Gingerich, D. S., Trzynka, A., David, L., Stagg, S. M. & Chapman, M. S. (2019). *eLife*, **8**, e44707.
Mietzsch, M., Penzes, J. J. & Agbandje-McKenna, M. (2019). *Viruses*, **11**, 362.
Mingozzi, F. & High, K. A. (2011). *Nat. Rev. Genet.* **12**, 341–355.
Mingozzi, F., Liu, Y.-L., Dobrzynski, E., Kaufhold, A., Liu, J. H., Wang, Y., Arruda, V. R., High, K. A. & Herzog, R. W. (2003). *J. Clin. Invest.* **111**, 1347–1356.
Mount, J. D., Herzog, R. W., Tillson, D. M., Goodman, S. A., Robinson, N., McCleland, M. L., Bellinger, D., Nichols, T. C., Arruda, V. R., Lothrop, C. D. Jr & High, K. A. (2002). *Blood*, **99**, 2670–2676.
Mueller, C. & Flotte, T. R. (2008). *Gene Ther.* **15**, 858–863.
Nam, H.-J., Gurda, B. L., McKenna, R., Potter, M., Byrne, B., Salganik, M., Muzyczka, N. & Agbandje-McKenna, M. (2011). *J. Virol.* **85**, 11791–11799.
Nam, H.-J., Lane, M. D., Padron, E., Gurda, B., McKenna, R., Kohlbrenner, E., Aslanidi, G., Byrne, B., Muzyczka, N., Zolotukhin, S. & Agbandje-McKenna, M. (2007). *J. Virol.* **81**, 12260–12271.
O'Donnell, J., Taylor, K. A. & Chapman, M. S. (2009). *Virology*, **385**, 434–443.
Orlova, E. V., Dube, P., Harris, J. R., Beckman, E., Zemlin, F., Markl, J. & van Heel, M. (1997). *J. Mol. Biol.* **271**, 417–437.
Pettersen, E. F., Goddard, T. D., Huang, C. C., Couch, G. S., Greenblatt, D. M., Meng, E. C. & Ferrin, T. E. (2004). *J. Comput. Chem.* **25**, 1605–1612.
Punjani, A., Rubinstein, J. L., Fleet, D. J. & Brubaker, M. A. (2017). *Nat. Methods*, **14**, 290–296.
Rose, J. A., Maizel, J. V., Inman, J. K. & Shatkin, A. J. (1971). *J. Virol.* **8**, 766–770.
Rosenberg, J. B., Sondhi, D., Rubin, D. G., Monette, S., Chen, A., Cram, S., De, B. P., Kaminsky, S. M., Sevin, C., Aubourg, P. & Crystal, R. G. (2014). *Hum. Gene Ther. Clin. Dev.* **25**, 164–177.
Subramanian, S., Organtini, L. J., Grossman, A., Domeier, P. P., Cifuente, J. O., Makhov, A. M., Conway, J. F., D'Abramo, A. Jr, Cotmore, S. F., Tattersall, P. & Hafenstein, S. (2017). *Virology*, **510**, 216–223.
Tang, G., Peng, L., Baldwin, P. R., Mann, D. S., Jiang, W., Rees, I. & Ludtke, S. J. (2007). *J. Struct. Biol.* **157**, 38–46.
Tseng, Y.-S. & Agbandje-McKenna, M. (2014). *Front. Immunol.* **5**, 9.
Wang, L., Calcedo, R., Wang, H., Bell, P., Grant, R., Vandenberghe, L. H., Sanmiguel, J., Morizono, H., Batshaw, M. L. & Wilson, J. M. (2010). *Mol. Ther.* **18**, 126–134.
Wang, L., Wang, H., Bell, P., McCarter, R. J., He, J., Calcedo, R., Vandenberghe, L. H., Morizono, H., Batshaw, M. L. & Wilson, J. M. (2010). *Mol. Ther.* **18**, 118–125.
Wang, Q., Lock, M., Prongay, A. J., Alvira, M. R., Petkov, B. & Wilson, J. M. (2015). *Mol. Ther. Methods Clin. Dev.* **2**, 15040.
Wu, M., Lander, G. C. & Herzik, M. A. (2019). *bioRxiv*, 855643.
Wu, Z., Asokan, A. & Samulski, R. J. (2006). *Mol. Ther.* **14**, 316–327.
Yang, B., Li, S., Wang, H., Guo, Y., Gessler, D. J., Cao, C., Su, Q., Kramer, J., Zhong, L., Ahmed, S. S., Zhang, H., He, R., Desrosiers, R. C., Brown, R., Xu, Z. & Gao, G. (2014). *Mol. Ther.* **22**, 1299–1309.
Zhang, H., Yang, B., Mu, X., Ahmed, S. S., Su, Q., He, R., Wang, H., Mueller, C., Sena-Esteves, M., Brown, R., Xu, Z. & Gao, G. (2011). *Mol. Ther.* **19**, 1440–1448.
Zhang, R., Cao, L., Cui, M., Sun, Z., Hu, M., Zhang, R., Stuart, W., Zhao, X., Yang, Z., Li, X., Sun, Y., Li, S., Ding, W., Lou, Z. & Rao, Z. (2019). *Nat. Microbiol.* **4**, 675–682.
Zheng, S. Q., Palovcak, E., Armache, J.-P., Verba, K. A., Cheng, Y. & Agard, D. A. (2017). *Nat. Methods*, **14**, 331–332.
Zivanov, J., Nakane, T. & Scheres, S. H. W. (2019). *IUCrJ*, **6**, 5–17.
Zolotukhin, S., Byrne, B. J., Mason, E., Zolotukhin, I., Potter, M., Chesnut, K., Summerford, C., Samulski, R. J. & Muzyczka, N. (1999). *Gene Ther.* **6**, 973–985.